

3 **Spatial and temporal structure of the fog life cycle**
4 **over Atlantic Canada and the Grand Banks**

5 **Adriana Formby-Fernandez¹ | Luc Lenain¹ | Nicholas
Pizzo² | Clive E. Dorman¹ | Shang-Ping Xie¹**

¹Scripps Institution of Oceanography,
University of California San Diego, La Jolla,
California, 92037, USA

²Graduate School of Oceanography,
University of Rhode Island, Narragansett,
Rhode Island, 02882, USA

Correspondence

Luc Lenain, Scripps Institution of
Oceanography, University of California San
Diego, La Jolla, California, 92037, USA
Email: llenain@ucsd.edu

Funding information

This work was supported by the Office of
Naval Research under grant
N00014-21-1-2825 and the National
Science Foundation Graduate Research
Fellowships Program (GRFP).

Marine fog impacts human health, naval strategy, and biological productivity. Despite its importance, the skill of operational and global environmental models in forecasting marine fog and its optical properties remain limited due to our incomplete understanding of the physical processes that drive fog, particularly over its broad range of temporal and spatial scales. In this work, we present findings from a 71-year climatological analysis covering a broad range of spatial and temporal scales of marine fog over Atlantic Canada and the Grand Banks of Newfoundland, Canada. Using ICOADS observations from 1950-2020, ERA5 reanalysis products, and satellite imagery, we discuss fog formation in this region. Spatially, the Atlantic Canada continental shelf induces submesoscale ocean features along its rapid variation in bathymetry, which influence fog formation. Sharp sea surface temperature gradients and air-sea temperature differences coincide with the over-the-shelf fog maxima in summer (June, July, and August). The air-sea temperature differences show a clear signal that fog occurrence is higher with negative air-sea temperature differences (SST - air temperature). This higher occurrence of fog is mainly isolated on the continental shelf, where colder SST typically exists. Satellite imagery of a fog event during the 2022 Office of Naval Research (ONR) funded Fog and Turbulence Interactions in the Marine Atmosphere (FATIMA)

Multidisciplinary University Research Initiative (MURI) campaign highlights the complicated interplay of shelf break dynamics and near-surface atmospheric conditions. A fog bank is shown to form in the colder water regions over the shelf, outlining the shelf break and pointing to boundary layer and smaller-scale processes that are driving fog formation. These observations are crucial in characterizing the spatial and temporal structure of the fog life cycle and provide a better understanding of fog occurrence in this region.

KEYWORDS

marine fog, air-sea interaction, atmospheric boundary layer, physical oceanography

1 | INTRODUCTION

Despite its societal importance, our understanding and ability to predict fog in coastal, offshore or in land environments remains limited. This is in part due to complexity of the multi-phase physical processes driving the fog life cycle and the observational challenges of characterizing processes that span a broad range of spatio-temporal scales (i.e. synoptic to microphysical turbulence scales). As fog reduces visibility at sea, improved understanding of the small-scale structure of fog, including aerosol, droplet and turbulence properties, is necessary in order to better forecast the propagation of optical and radio-frequency electromagnetic signals critical to operations at sea (both for aircraft and vessels).

Fog is defined as a collection of airborne water particles or ice crystals of magnitude 5-50 μm that collectively reduce visibility to less than 1 km near the Earth's surface (Gultepe et al., 2007). Fog can exist over land or water and has been categorized into 11 main types (Willett, 1928; Byers, 1959) depending on formation mechanism and location. This study explores advection marine sea fog, which occurs when warmer, higher humidity air is advected over colder sea surface regions (Gultepe et al., 2007). The warmer air cools and condenses to become fog, extending from the ocean surface to up to several hundreds meters in height (see Figure 1). The fog life cycle is constrained by a range of multiscale processes both in the atmosphere and at the air-sea boundary: radiative cooling at the fog top, the evolution of surface heat and turbulent moisture fluxes resulting from flows over ocean fronts, and other variations in turbulence within the cloud (Findlater et al., 1989; Yang and Gao, 2020). Radiative cooling and turbulent mixing of the overlying warm air leads to a more thermally stable internal boundary layer. This persists because the marine boundary layer (MBL) is divided into two regions: 1) a turbulent layer near the sea surface due to mechanical drivers (e.g. shear turbulence), and 2) a thermal radiation layer from long-wave cooling of the fog top (Koraćin et al., 2014). Vertical mixing increases within the MBL when air blows over a warm-to-cold SST front. The vertical mixing is due to instabilities triggered by the change in air-sea temperature difference. This allows the MBL to deepen and allows for more entrainment at the top of the MBL (Skylingstad et al., 2007).

Fog formation is influenced by a combination of synoptic large scale weather patterns (Koraćin and Dorman, 2017) and small-scale, local microphysical processes, making fog prediction and modeling particularly challenging (see, e.g. Wainwright and Richter, 2021; Chen et al., 2021; Pithani et al., 2019; Taylor et al., 2021; Hu et al., 2014;

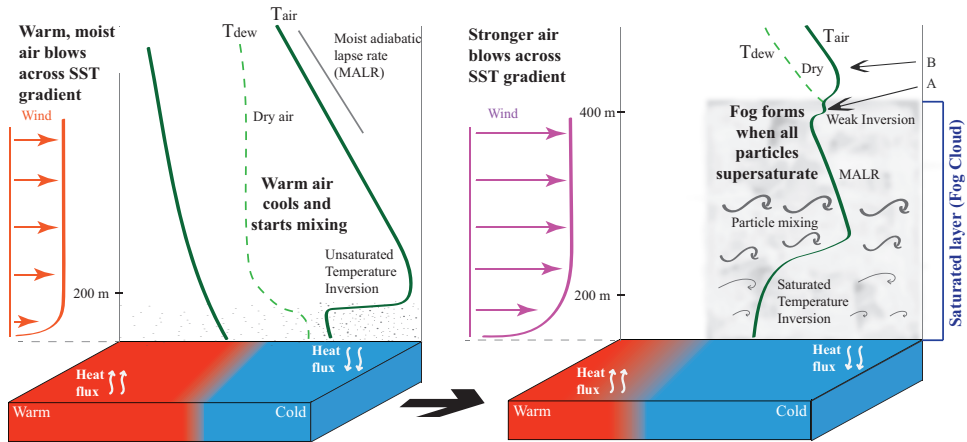


FIGURE 1 Simplified schematic of warm advection sea fog formation over a cold boundary, such as a shelf break. In the first panel, normal summer conditions are shown: low-level unsaturated temperature inversion with dry air aloft, and cooling particles that are not saturated. The second panel shows conditions favorable for fog following an atmospheric trigger: a saturated, low-level temperature inversion below a weaker inversion (A) with dry air aloft (B). Stronger and more turbulent wind causes particle mixing within a deeper and saturated layer in which fog can form.

32 Park et al., 2022). Typically atmospheric temperature decreases with height. A temperature *inversion* exists when
 33 temperatures above the sea surface increase with height. During normal summer conditions over the ocean, a low-
 34 level, near surface temperature inversion exists with unsaturated air parcels. This marine boundary layer is stable,
 35 such that convective motions between the layers are not expected (Nieuwstadt, 2005). Within the boundary layer,
 36 horizontal movement of warm air over colder water creates and maintains an air temperature inversion, creating a
 37 stratified layer between the sea surface and the boundary layer above. Winds blowing across an SST gradient, as
 38 shown in Figure 1, result in the cooling of the sea surface and boundary layer such that saturation is not achieved. If
 39 the dominant mean condition is a moist but unsaturated surface-based air temperature inversion, with drier air above,
 40 winds from the warm side of the SST gradient with wind shear and turbulence increasing from the sea surface upward,
 41 then a trigger is needed to convert this mean unsaturated surface air temperature inversion to a saturated surface air
 42 temperature inversion. This trigger could be a mid-level trough axis crossing overhead, causing surface convergence
 43 in the boundary layer and an increase in the surface wind speed and greater wind shear in the boundary layer. The
 44 surface convergence generates a lift that extends the shallow moist boundary layer to a deeper, saturated layer with a
 45 surface air temperature inversion below a layer with a saturated adiabatic lapse rate (labelled MALR in Figure 1). This
 46 saturated layer is much deeper than the preceding, unsaturated but moist air temperature inversion. Finally, there
 47 can be a weak saturated air temperature inversion at the top of the saturated layer, denoted by A in the right panel of
 48 Figure 1. Above the weak inversion is another smaller inversion (denoted by B) that shows where the dry air begins
 49 above the fog cloud. The transition from unsaturated to a saturated surface boundary layer is not well documented
 50 and understood, though horizontal convergence and shear turbulence are likely playing a role in this process. In any
 51 event this usually occurs within a stable surface layer wherein moisture is moved upward in a stable layer to cause
 52 saturation, which defies conventional expectations. This process through narrow layers that are temporarily unstable,
 53 with Kelvin-Helmholtz billowing and mixing that moves moisture upward, can make the layer return to being stable,
 54 in a process described in Fernando et al. (2023). When the surface and atmospheric conditions are met, fog is formed.

To the north of the Gulf Stream and the Kuroshio currents are the world's most fog-prone regions (Dorman et al., 2017). These regions coincide with sharp ocean sea-surface temperature (SST) gradients and regions of energetic sub-mesoscale activity. The Grand Banks of Newfoundland, Canada, experiences a maximum of fog occurrence in June, July, and August (45%) and a minimum in December, January, and February (13%) with the greatest occurrences over the continental shelf (Dorman et al., 2020). This is a dynamically rich region of the western Atlantic, with cold water from the Labrador Current meeting the warmer waters of the Gulf Stream. These currents then interact with the continental shelf and predominant southwesterly atmospheric winds which advect relatively warm air over these cooler waters. In discussing a trip to the Grand Banks region in 1917, G.I. Taylor (Taylor, 1917) noted that he experienced 141 events of fog within the 804 days of the trip (including transit time to and from England). Prior to this, other accounts going back as far as 1823 (Scoresby, 1823) and 1907 (Brodrick, 1907) comment on the consistency of fog in the Grand Banks region during the summer. However, detailed spatial and temporal remote and in-situ measurements of these conditions were not historically available, motivating large field programs recently to study the fog life cycle through the lens of both synoptic meteorologists and micro-scale atmospheric scientists (Dorman et al., 2020, 2021; Wainwright and Richter, 2021; Isaac et al., 2020; Gultepe et al., 2009; Dimitrova et al., 2021; Fernando et al., 2021) with the aim of understanding fog dynamics.

Several recent projects, such as the Fog and Turbulence Interactions in the Marine Atmosphere (FATIMA) project, the C-FOG project (Fernando et al., 2021), and the Fog Remote Sensing and Modeling (FRAM) project (Gultepe et al., 2009) have set out to improve understanding of fog dynamics and forecasting through a better understanding of the impact of smaller scale processes on the fog life cycle. FRAM was a three-part field campaign that explored continental and coastal fog in Canada in which in-situ and remote sensing observations were collected. C-FOG was a multidisciplinary project that sought out to investigate coastal fog from multiple lenses, including air-sea interaction processes, thermodynamics, microphysics, and dynamics. This campaign included a field deployment in Nova Scotia and Newfoundland, from September to October 2018, in which various instruments collected atmospheric and oceanic variables to include in improved numerical models of the fog life cycle. C-FOG was able to highlight the need for further implementation of fog physics at smaller scales into models and forecasting schemes. This project led to the Office of Naval Research (ONR) funded Fog and Turbulence Interactions in the Marine Atmosphere (FATIMA) Multidisciplinary University Research Initiative (MURI) program, that included a field campaign in that same region in July 2022 to explore fog from synoptic to microphysical scales. In-situ observations were collected during the foggiest time of year in this region for optimal conditions to investigate the fog life cycle.

Coinciding with the locations of highest fog occurrence in this region is a cold sea surface temperature signature aligned with the shelf break. The link between the location of high fog occurrence and the boundary of the shelf break in the Grand Banks region (see figure 3a) motivates this work. In particular, understanding the oceans' role in providing a crucial surface boundary condition to the atmosphere is vital to being able to understand this phenomenon as completely as possible (Fallmann et al., 2019).

This study aims to provide a broad perspective of the multi-scale air-sea interactions that are associated with the fog life cycle that are driven by the atmospheric and oceanic properties. We present a novel outlook on advection sea fog through a 71-year climatological analysis of fog occurrence and its sufficient components over the Grand Banks region coupled with a small-scale investigation of an individual fog event over Sable Island. It is important to evaluate the impact that the surface conditions have on fog, so that models and forecast schemes can accurately predict this phenomenon. We find that the ocean plays a crucial role in the fog life cycle through its impact on the surface boundary conditions needed for advection sea fog formation.

The oceanographic context of the Grand Banks Region is described in Section 2. Section 3 explains the data and methods used in this study. Section 4 presents the results. Section 5 summarizes and discusses the findings from this

98 paper.

99 2 | OCEANOGRAPHIC CONTEXT OF THE GRAND BANKS REGION

100 The Atlantic Canada shelf is positioned at a crucial location in the earth climate system where different water masses,
 101 from the colder fresher Labrador Current water to the warmer Labrador Sea water and the warm Gulf Stream water,
 102 interact above and along the continental shelf break, leading to complex and variable dynamical interplay that modu-
 103 late the regional ecosystem (Loder, 1998; Richardson et al., 2001; Talley, 2011; Ricketts et al., 1931; Fratantoni and
 104 Pickart, 2007; Clarke et al., 1980; Sheng and Thompson, 1996; Han et al., 2011). The Labrador Current brings in cold
 105 and fresh water from the Labrador Sea into the Grand Banks region (Fratantoni and Pickart, 2007; Clarke et al., 1980)
 106 over the Scotian Shelf, and south towards Cape Hatteras. There are two main outflow points, the first one at Flemish
 107 Pass (at the northern edge of the Grand Banks) and the second one at the Tail of the Grand Banks (at the southern
 108 edge) (Fratantoni and Pickart, 2007; Petrie and Anderson, 1983). The current that dominates the southern part of this
 109 region is the Gulf Stream, which becomes the North Atlantic Current (NAC) further to the east (Clarke et al., 1980).
 110 The Gulf Stream splits into three branches: 1) a southward stream that goes equatorward along the outer boundary
 111 of the original Gulf Stream, 2) a southeastward portion of the North Atlantic Current that eventually becomes the
 112 Azores Current, and 3) a northeastward portion that becomes the North Atlantic Current. This third branch is the
 113 most relevant to this study, as this is the section closest to the Grand Banks (Talley, 2011). As the Gulf Stream moves
 114 north and east, it splits into smaller features, such as the Mann Eddy, the North Recirculation Gyre, and other eastward
 115 propagating currents.

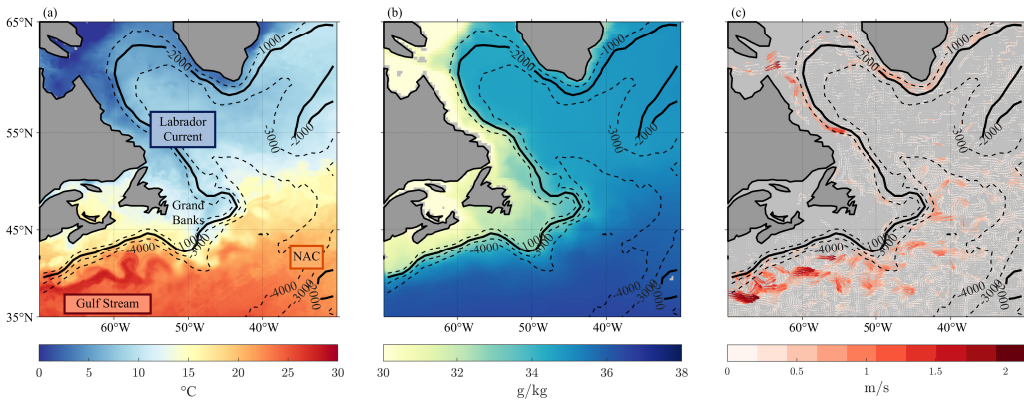


FIGURE 2 (a) Mean SST map from the Group for High Resolution Sea Surface Temperature (GHRSSST) Multiscale Ultrahigh Resolution (MUR) Level 4 products showing the Labrador Current and Gulf Stream interaction over the Grand Banks from July 10, 2022 2100Z to July 11, 2022 2100Z. (b) Mean Salinity from the Ocean Reanalysis System 5 (ORAS5) data from July 1958-2020. (c) Atlantic Oceanographic and Meteorological Laboratory (AOML) Surface Drifter currents for July 2012-2022 (Lumpkin and Centurioni, 2019). Contour lines for bathymetry are set for every 1000 m down to 4000 m. The 2000 m depth contour is slightly thicker for clarity, as this will be the reference contour for the rest of the paper. NAC: North Atlantic Current

116 This splitting of the Gulf Stream induces complex dynamics involving smaller scale processes. The meanders and
117 jets associated with the Gulf Stream Extension are highly energetic. Figure 2c shows some of these meanders and jets
118 occurring just south of the Grand Banks. This is also seen in the 24-hour composite of the sea surface temperature in
119 Figure 2a. The sea surface salinity shows a clear division between the fresh water on the shelf and the saltier water
120 off shelf (Figure 2b). Figure 2c shows the complexity of the surface currents east of the shelf, where the water exiting
121 the Gulf Stream merges with the Labrador water flowing southward. As the surface currents from the Gulf Stream
122 are driven northward due to winds, this warmer, saltier water is able to mix and interact with the colder shelf water.
123 This creates a region where mesoscale and energetic submesoscale activity is heightened and supported. With the
124 presence of sharp, submesoscale features (McWilliams, 2016) found near the continental shelf (Bower et al., 2013),
125 increased air-sea interactions is expected (Su et al., 2018). These air-sea interactions involve the exchange of heat
126 between the atmosphere and ocean. In particular, it has been established that the air-sea temperature difference is a
127 driving mechanism for advection fog formation (Gultepe et al., 2007; Wainwright and Richter, 2021; Isaac et al., 2020;
128 Dorman et al., 2020).

129 3 | DATA AND METHODS

130 A combination of in-situ (e.g. ship, autonomous surface vehicles, platforms, buoys) and remote sensing observations
131 are used in this analysis, along with two reanalysis products (ERA5 and ORA5). They are described below.

132 3.1 | ICOADS Archive

133 Following the approach of Dorman et al. (2020), we used archived observations as part of the International Com-
134 prehensive Ocean and Atmospheric Dataset (ICOADS) (Freeman et al., 2017) v3.0.0. This archive combines global
135 in-situ observations collected from ships, buoys, and other ocean-based platforms since 1662. Here we use a subset
136 of observations spanning from January 1, 1950 through December 31, 2020 over the region of Grand Banks and the
137 northwest Atlantic, from 35-65°N and 30-70°W. For reference, figure S1 (supporting information) shows the density
138 of observations binned in binned in 1°x 1° used in this analysis, along with the type of platforms that recorded these
139 observations (figure S2). Sampling rates varied greatly throughout the span of the record, ranging from subhourly to 3-
140 hour intervals. Due to the nature of the dataset, i.e. a combined record from all vessels in the area, some observations
141 occurred within a few seconds of each other, while others were taken only daily. For this analysis, the time sampling
142 was not an issue as data is averaged monthly. Monthly average maps of selected variables are over a 1°x 1° grid, while
143 observations from on and off the shelf are averaged spatially in different subregions to analyze the temporal evolu-
144 tion of the state variables and fog over the course of the 71-year record. To compute fog occurrence, we divide the
145 number of present weather observations categorized as "fog" (ICOAD codes 40-49) over the total amount of present
146 weather observations within the 1°x 1° grid box. These codes follow from the WMO Code Table 4677 (WMO, 2019;
147 Dorman et al., 2020). The 2000 m depth contour is used to identify the location of the continental shelf break in the
148 figures.

149 The ICOADS observations are quality controlled using the NCDC QC flags. Specific thresholds to remove outliers
150 are added as a secondary check. These criteria are shown in Table 2. Observations where sea surface temperature
151 (SST) and surface air temperature (SAT) is above 35°C or below -5°C are removed. The difference between SST
152 and SAT (ΔT) is also limited to -10°C and 10°C. The surface wind speed upper threshold is set at 30 m/s to limit
153 contributions from energetic storms in the climatology.

TABLE 1 ICOADS variables used with their respective resolutions. The time resolution is variable due to the nature of the dataset being collected from many sources. ERA5 single level data is taken from the surface (or lowest level available). ERA5 pressure level data includes all the levels in the atmospheric model. ORAS5 data is taken from 0-10 m depth.

Period Covered	Time Resolution	Grid Resolution	Variable	Units
ICOADS v3.0.0				
1950-2020	Variable	1°x 1°	SST	°C
			Air Temperature	°C
			Present Weather (WW)	N/A
			Wind Speed (W)	m/s
			Wind Direction (D)	°
1950-2014			Salinity (OSV)	g/kg
ERA5 Single Level				
1950-2020	Hourly	0.25°x 0.25°	SST	°C
			Air Temperature	°C
			Surface Latent Heat Flux	kW m ⁻²
			Surface Sensible Heat Flux	kW m ⁻²
ERA5 Pressure Levels				
1950-2020	Hourly	0.25°x 0.25°	Air Temperature	°C
			Air Pressure	mb
ORAS5				
1958-2020	Monthly	0.25°x 0.25°	Potential Temperature	°C
			Salinity	PSU

154 3.2 | ECMWF ERA5 and ORA5 reanalysis products

155 The ICOADS dataset is augmented with hourly, gridded products from the ECMWF Reanalysis v5 (ERA5) (Hersbach
 156 et al., 2018) products for 1950-2020. A list of all considered variables is included in Table 1. Additional ocean state
 157 products are also obtained from the ORAS5 Global ocean reanalysis monthly data from 1958-2020 (Zuo et al., 2018).
 158 All reanalysis data is averaged through all years for each corresponding month within a 0.25° by 0.25° grid box.

159 3.3 | ONR FATIMA 2022 field program

160 The first campaign of the ONR FATIMA MURI program occurred from July 3rd to August 3rd, 2022 in the Grand Banks,
 161 combining observations from a research vessel, autonomous surface vehicles (Grare et al., 2021), and an extensive
 162 suite of atmospheric sensors installed on Sable Island, including a ceilometer CL31 used in the present analysis.

TABLE 2 Quality check and additional thresholds and criteria set on the ICOADS data to ensure storm bias and other errors were not included in the analysis.

Variable	Quality Check Variable Name	Threshold Criteria
ICOADS v3.0.0		
SST	SNC	-5 to 35°C
Air Temperature	ANC	-5 to 35°C
Present Weather (WW)	XNC	Fog Code = 40-49
Wind Speed (W)	WNC	0-30 m s ⁻¹
Wind Direction (D)	WNC	N/A
Salinity (OSV)	N/A	0-10 m depth

163 3.4 | GOES geostationary satellite (GOES-16) observations

164 Geostationary Operational Environmental Satellites (GOES) 16 is a satellite operated by NASA and the National
 165 Oceanic and Atmospheric Administration (NOAA). GOES-16 serves as the operational geostationary weather satel-
 166 lite in the GOES East position at 75.2° W, providing a view centered on North America, extending to the Atlantic and
 167 Pacific oceans with a nominal 2 km and 5 minute spatial and temporal resolution. GOES-16 provides observations
 168 both in the visible and infrared wavelength through 16 spectral bands (Advanced Baseline Imager - ABI). Following
 169 the approach of Amani et al. (2020), we use two of these ABI bands, the thermal infrared (~11 μm) and mid-infrared
 170 (~3.9 μm), to compute brightness temperature difference by subtracting the thermal infrared band by the mid-infrared
 171 band. The thermal infrared band shows a higher brightness temperature for fog than the mid-infrared band, but clouds
 172 appear the same in both. After subtracting the two bands, clouds are removed and fog can be more clearly seen, if
 173 there are no clouds above the fog layer. The algorithm is modified to enable daytime fog detection by adjustments
 174 made to the detection threshold, following the approach described in Mahdavi et al. (2020).

175 4 | RESULTS

176 4.1 | July Fog climatology over the Grand Banks region

177 Observational data from 1950-2020 from ICOADS and ERA5 is analyzed spatially to characterize the climatology of
 178 fog within this region. The mean monthly spatial patterns present for fog occurrence and other surface conditions for
 179 July are shown in Figure 3. We find that the high probability of fog occurrence (over 20% of the time) is concentrated on
 180 the Grand Banks continental shelf region, with a sharp drop in fog occurrence remarkably collocated with the location
 181 of the shelf break (denoted by the 2000 m depth contour in black) in Figure 3a. This region of high probability of
 182 occurrence on the shelf coincides with negative air-sea temperature differences (Figure 3b). The air-sea temperature
 183 difference (ΔT) is defined as SST minus surface air temperature. We find that fog occurs over 40% of the time on
 184 the shelf, with some areas experiencing up to 60%. The sharp delineation between the high fog occurrence zone on
 185 the shelf is most prevalent on the south side of the Grand Banks. Very limited occurrence of fog is found south of
 186 the shelf. This is complemented with an equally sharp delineation of air-sea temperature differences on and off the

187 shelf. Figure 3b shows this with negative values (down to -2°C) on the shelf, and positive values off the shelf (up to
 188 $+2^{\circ}\text{C}$). There is a remarkable correlation between the locations of the continental shelf break and the region where
 189 the air-sea temperature difference changes sign. This clear spatial pattern on and off the shelf is also seen in the sea
 190 surface (Figure 3c) and surface air temperature (Figure 3d) maps. From these, the cold temperature signature is seen
 191 occurring on the shelf and to the north of the Grand Banks. The warm Gulf Stream is clearly seen to the south of
 192 the shelf. The gradual warming of the air temperature across the shelf versus the stronger temperature gradient of
 193 the sea surface at the shelf break is the main contributor to the sharp air-sea temperature difference along the shelf
 194 break.

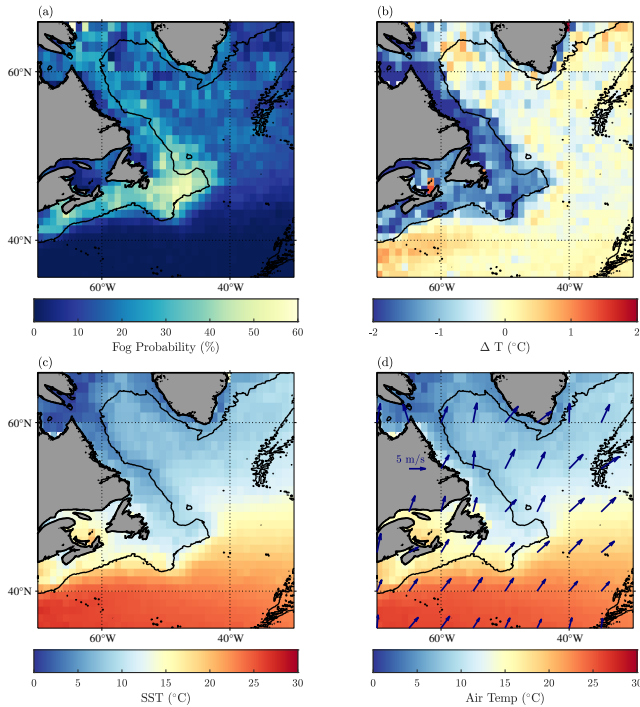


FIGURE 3 ICOADS July maps from averaged $1^{\circ}\times 1^{\circ}$ boxes across 71 years of data. (a) Fog Occurrence. (b) Average Air-Sea Temperature Difference (ΔT) per grid point in $^{\circ}\text{C}$. (c) Average SST per grid point in $^{\circ}\text{C}$. (d) Average Air Temperature per grid point in $^{\circ}\text{C}$ with the average wind overlaid in dark blue.

195 Mean wind direction for the month of July is shown overlaid in Figure 3d. Note, wind observations archived in
 196 ICOADS are subject to height measurement bias, that are not accounted here. The wind is generally coming from the
 197 southwest, with monthly averaged wind speed ranging from 1 to 14 m/s, bringing warm air above the much colder
 198 waters present on the shelf. These conditions enable the generation of the negative air-sea temperature difference
 199 on the shelf.

200 Here we find that the regions with highest fog occurrence are concurrently found in regions of negative air-sea
 201 temperature differences and wind that brings in warmer air over colder water. The surface boundary conditions
 202 present during July allow for more opportunities of fog formation, which is proven by the high fog probability of

203 occurrence. Previous work done in this region confirms the existence of this optimal setup during July (Dorman et al.,
 204 2020, 2021).

205 4.2 | May through August fog climatology over the Grand Banks region

206 Extending the climatological analysis to encompass the northern hemisphere summer, we present the fog probability
 207 of occurrence and air-sea temperature differences for May, June, July, and August in Figure 4, with each column
 208 corresponding to a different month. Fog occurrence increases from May through July, with the peak in July (up to
 209 60%, Figure 4c) as previously shown. The fog probability of occurrence decreases in August, down to less than 40%.
 210 In July, a significant amount of fog (20-25%) also occurs in the higher latitudes within the Labrador Current, hinting at
 211 either the role of local submesoscale processes in this region extending away from the shelf or due to synoptic scale
 212 patterns interacting with the land and the ocean. Regardless of the month, fog occurrence remains limited off the shelf
 213 to the south of the Grand Banks. Along with this temporal trend in fog probability of occurrence, we find that negative
 214 air-sea temperature differences coincide with areas of high fog occurrence in each of the months. From May through
 215 July, we see a decrease in the magnitude of the air-sea temperature difference (Figure 4e through g) associated with
 216 a slow seasonal warming of the waters on the shelf. Coincident with decreasing occurrence of fog, the magnitude
 217 of air-sea temperature difference increases in August as the continent starts to cool slightly earlier than the ocean
 218 (Zhang et al., 2009) (see subsection 4.3). This relationship between fog probability of occurrence and the magnitude
 219 of air-sea temperature difference is further explored in Figure 5.

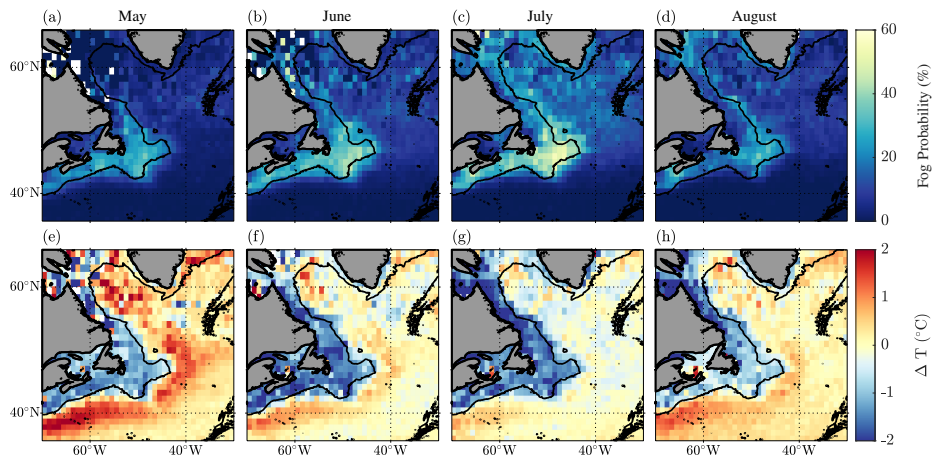


FIGURE 4 Spatial and temporal variability of fog occurrence (top row) and air-sea temperature difference (ΔT , second row). The air-sea temperature difference is defined as the SST minus the surface air temperature. The first column is for May, second is for June, third is for July, and the fourth column is for August. The 2000 m depth contour is shown.

220 Figure 5 shows the fog probability of occurrence averaged within a box located on the shelf, from 43°N to 47°N
 221 and -51°W to -43°W, binned in 0.5°C air-sea temperature difference increments. We find a negative correlation of
 222 fog probability with air-sea temperature differences. Each month shows this correlation pattern with a decrease in
 223 fog probability from at least -2°C to 1°C. May is a slight exception, with a consistent decrease in fog regardless of the

224 air-sea temperature difference. The maximum amount of fog probability occurs in July when the air-sea temperature
 225 difference range is between -4°C and -2°C . However, each month shows this pattern of highest fog probability within
 226 this air-sea temperature difference range. The temporal pattern of fog probability increasing from May to July, and
 227 decreasing in August, is also seen in this analysis (as shown in Figure 4).

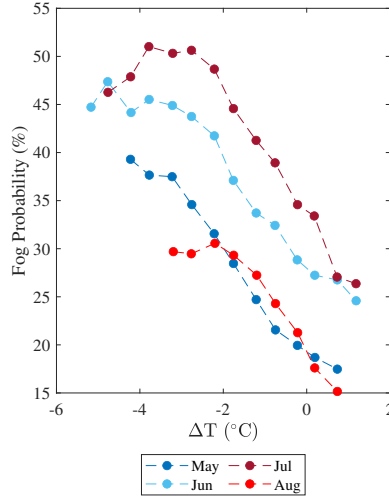


FIGURE 5 Fog occurrence with respect to varying air-sea temperature difference (ΔT) values for July.

228 Overall, fog occurs more frequently when the temperature gradient across the air-sea interface is largest. This is
 229 partly due to the transfer of heat, in which cooler water chills the air particles above it, making them condense, releas-
 230 ing more latent heat, and increasing their buoyancy. As these particles become more buoyant they rise, eventually
 231 forming a stably stratified layer in which fog can form. The threshold for this temperature gradient has been examined
 232 in LES models (Wainwright and Richter, 2021). In July, warmer air from the Gulf Stream tends to blow over the Grand
 233 Banks, and thus intensifies the negative air-sea temperature differences which can cause greater fog occurrence.

234 We have shown that the surface conditions during the summer months in the Grand Banks have an impact on
 235 the amount of fog occurrence. Fog formation and existence is dependent on air-sea differences, as well as favorable
 236 atmospheric conditions. The heat and energy exchange between the ocean surface and the atmosphere are critical
 237 for sea fog formation. In particular, surface latent and sensible heat fluxes can indicate regions that are consistent
 238 with fog formation and dissipation.

239 A climatology of monthly averaged surface latent and sensible heat fluxes obtained from ERA5 over the 71-year
 240 record used for the analysis of the ICOADS data are shown in Figure 6. These fluxes are positive into the ocean.
 241 Positive latent heat flux corresponds to conditions where water is condensing in the lowest section of the atmosphere,
 242 and negative values indicate evaporation from the sea surface. On the shelf, we find the small surface latent heat flux
 243 to be positive where particles are releasing latent heat through condensation (Severini et al., 1986) into a stable
 244 boundary layer with visibilities mostly in the range of 1-10 km (Gultepe et al., 2009). Most of this heat is lost through
 245 sensible heat back to the colder ocean surface. Further, during all conditions, moisture droplets in the usually very
 246 stable surface boundary layer are moved upward into the drier air above by a process proposed by Fernando et al.

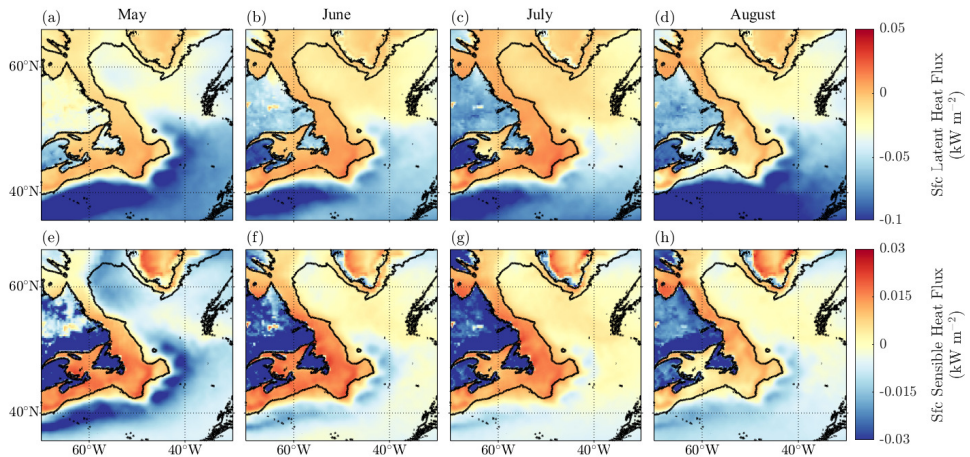


FIGURE 6 Average Surface Latent Heat Flux (kW m^{-2}) (top row) and Surface Sensible Heat Flux (kW m^{-2}) (bottom row) for May to August from 1950-2020 from ERA5. Positive fluxes are into the ocean. The 2000 m depth contour is shown.

247 (2023) which explains why the summer stable marine boundary layer is not saturated all the time.

248 The role of sensible heat flux in the context of the fog life cycle has been extensively studied (e.g. Yang et al.
249 2019; Thompson et al. 2005; Yun and Ha 2022). Positive sensible heat flux within fog or cloudy conditions acts as
250 dissipation of the feature. Again, positive values indicate fluxes into the ocean for this analysis. In Figure 6(e-f) we
251 find that higher positive values of surface sensible heat are found on the shelf, correlated with the areas of negative
252 air-sea temperature differences and high fog occurrence. In particular, the surface sensible heat flux denotes areas
253 where fog dissipation is occurring more frequently. South of the shelf, we find negative sensible heat fluxes, which
254 show where the Gulf Stream brings warm water to that region.

255 From this summer analysis of the climatology of the Grand Banks region, we find that the surface conditions con-
256 tribute to the occurrence of fog. A stronger air-sea temperature difference directly correlates to higher fog occurrence.
257 Similar spatial and temporal patterns of surface heat fluxes show the interaction between the air-sea interface, which
258 aids in fog formation or dissipates existing fog events.

259 4.3 | Monthly climatology over the Grand Banks region

260 To further explore the impact of the surface conditions on fog occurrence, a monthly climatology of key variables
261 in the fog life cycle is shown in Figure 7. A combination of ICOADS, ERA5, and ORAS5 data is used to show a
262 broad perspective of the average conditions found during each month from 1950-2020. These variables include the
263 fog probability of occurrence (from ICOADS), the probability of occurrence of atmospheric temperature inversions
264 (from ERA5), sea surface temperature (from ICOADS), surface air temperature (from ICOADS), air-sea temperature
265 difference (from ICOADS), wind speed and direction (from ICOADS), and salinity (from ORAS5). These averages are
266 computed over two small regions on the shelf (blue, 51°W to 48°W and 45°N to 48°N) and off the shelf (red, 55°W
267 to 52°W and 39°N to 42°N).

268 The July and summer climatologies show the correlation of surface variables, such as sea surface temperature,

269 surface air temperature, and winds on fog probability of occurrence. The surface conditions impact surface heat
270 fluxes, and the spatial variation of these variables correlates with the fog probability of occurrence. Warm season
271 marine fog depends critically on the presence of a stable layer in the lower atmospheric boundary layer (Dorman
272 et al., 2017). Usually this is a surface-based, or near surface-based air temperature inversion but could be an isothermal
273 layer (Dorman et al., 2024). The presence of an inversion layer is computed from ERA5 atmospheric profiles that are
274 averaged per month over the 71-year record considered. For each hourly atmospheric profile, the pressure levels
275 during the occurrence of temperature inversion ($\frac{dT}{dz} > 0$) is identified. The fraction of times when this occurs is then
276 computed per month. Figure 7 shows the components sufficient for fog occurrence for each month.

277 The fog probability of occurrence (Figure 7a) shows a clear difference between on (blue) and off (red) shelf fog
278 amounts during the summer months, experiencing up to 50% of fog on the shelf, and less than 10% of fog off the
279 shelf. The temporal pattern of an increase in fog probability starting in April, peaking in July, and decreasing in August
280 is shown in the on shelf (blue) line.

281 The probability of occurrence of temperature inversions on (Figure 7b) the shelf show the existence of low-level
282 (below 500 m) temperature inversions up to 80% of the time on the shelf during the summer. In contrast off the shelf
283 (Figure 7c), only 200 km away, we find temperature inversions limited to less than 15%, and extending to much larger
284 altitudes (1000-2000 m) and quasi nonexistent during the late July-August.

285 The sea surface (Figure 7d) and surface atmospheric temperatures (Figure 7e) follow an expected pattern of
286 warmer temperatures in the summer months. The cooler temperature signature expected on shelf from the influence
287 of the Labrador Current is seen in both panels. The warmer temperatures off shelf are from the Gulf Stream. The
288 difference between the two variables (Figure 7f) shows an interesting pattern in which the on shelf (blue) averages
289 are much lower in magnitude than the off shelf (red) ones, and becomes negative in the summer months. As previously
290 discussed, warm advection sea fog forms more often when the air-sea temperature difference is negative, which is
291 being shown here.

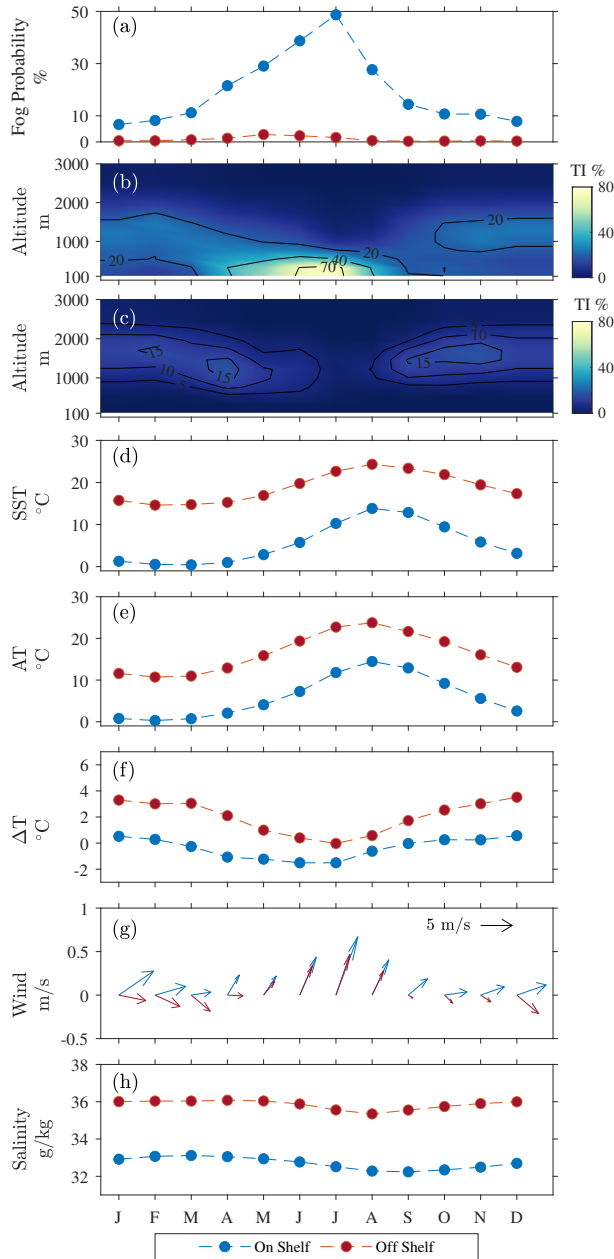


FIGURE 7 Monthly-averaged climatology from 1950-2020 on shelf (blue) and off shelf (red) for (a) Fog probability of occurrence from ICOADS data. (b) On shelf Temperature Inversion probability of occurrence from ERA5 data. (c) Off Shelf Temperature Inversion probability of occurrence from ERA5 data. (d) Average SST in °C from ICOADS data. (e) Average Air Temperature in °C from ICOADS data. (f) Average Air-Sea Temperature Difference in °C from ICOADS data. (g) Average winds in m/s from ICOADS data. (h) Average Salinity in g/kg from ORAS5 data.

292 The surface wind properties in Figure 8g show an interesting change in wind direction across the year. In January
293 to April, a clear difference in the angle between the on and off shelf winds are seen. This is also seen in September
294 through December. From May to August, during the months with the highest fog occurrence, the wind vectors on and
295 off shelf are aligned. This is evidence that the wind is blowing warm air from over the Gulf Stream over the shelf break
296 onto the cold water on the shelf. This is contributing to the air-sea temperature difference, aiding in the existence of a
297 low-level temperature inversion, and providing sufficient conditions for fog formation. The strongest winds occurring
298 in July further set-up fog formation by providing the turbulence needed for saturation and particle mixing.

299 The monthly-averaged salinity computed from ORAS5 in Figure 7h highlights the difference in ocean surface
300 properties between the two subregions. For the on shelf (blue) subregion, the salinity ranges from 32 and 34 g/kg. It
301 becomes slightly fresher from May through August, likely due to contribution from summer melting of sea ice to the
302 north, freshwater discharge from rivers, and general seasonal advection of the fresher Labrador Current water further
303 south (Hu and Zhao, 2022). This is shown slightly in the off shelf (red) subregion during this same time frame. Off
304 shelf, the salinity is much higher, around 36 g/kg, with some modulation in the late summer.

305 Ultimately, we find that as the water on the shelf continues to warm throughout the season, the difference in
306 temperature from the air brought in by the southwesterly winds and the ocean sea surface temperature decreases.
307 The monthly-averaged winds vary only slightly in magnitude and direction between July and August, hinting at the
308 role of ocean surface conditions in driving fog generation during the summer season. When this air-sea temperature
309 difference becomes smaller in magnitude (less negative, or zero), the marine boundary layer becomes more neutral,
310 decreasing convective motion within the layer, and limiting fog formation. As the air-sea temperature difference
311 becomes positive, the marine boundary layer is considered unstable and advection sea fog formation continues to be
312 limited. While this climatology provides insight into the importance of surface boundary conditions for fog formation,
313 the scales associated with changes to these conditions vary widely. The ocean sea surface temperature changes occur
314 on different time and space scales than winds and air temperature changes. This motivates the analysis presented in
315 the next section, which explores an individual fog event, captured with high temporal and spatial resolution.

316 4.4 | High-resolution observations of a fog event near Sable Island during the FATIMA 317 field campaign

318 To investigate the smaller-scale impacts of the surface conditions on fog, high resolution observations of an individual
319 fog event are analyzed. This event was selected as it corresponds to a period of time during the FATIMA field program
320 when the region was clear of high-level clouds, in turn enabling orbital observations of both fog and SST near Sable
321 Island, where the in-situ observations were collected. Based on the in-situ observations, this is a representative
322 example of a fog event in this region.

323 A ceilometer mounted at the South Tower on Sable Island provided observations of the structure of the atmo-
324 spheric boundary layer during the FATIMA 2022 experiment (Fernando et al., 2024). Measurements collected from
325 July 10, 2022 00:00 UTC to July 11, 2022 06:00 UTC are shown in Figure 8a, identifying an initially intermittent
326 shallow fog layer (from 20-150 m in depth off the surface) that lasted for close to 30 hours.

327 Fog spatial extent, computed from the GOES imagery product, along with coincident and collocated in-situ im-
328 agery of fog conditions collected from the South Tower at Sable Island, are presented for specific times (07/10/2022
329 17:47 UTC, 07/10/2022 20:06 UTC, 07/10/2022 23:32 UTC, 07/11/2022 01:01 UTC, and 07/11/2022 03:32 UTC)
330 in Figure 8(i-iv). The red dot in the satellite imagery on the left represents the location of Sable Island, while the white
331 dot represents the position of an instrumented wave glider deployed as part of the experiment (Grare et al., 2021);
332 white arrows are used to show wind direction and relative magnitude during these times. The fog extent is overlaid

333 on top of the mean SST from July 10-12, 2022 which was computed from averaged brightness temperature (ABI
334 band 14) for areas not contaminated by clouds or fog over the 48 hours considered. Though the 2-day averaging
335 leads to some smoothing, we can clearly identify submesoscale features such as filaments and fronts. The warmer
336 waters typically follow the shelf break though submesoscale features extend to the north and south of it, and are
337 more generally also located throughout the region. This includes the colder water on the shelf, and around Sable
338 Island, where island wakes are present. Note, fog dissipation and the generation of a fog-free region downstream of
339 the island is associated with the development of a daytime thermal internal boundary layer that grows with distance
340 from the leading shoreline Bardoel et al. (2024). Both orbital, in-situ and visual imagery products were collected at
341 the same time. The fog event in Figure 8 shows the following:

- 342 (i) 07/10/2022 17:47 UTC: The ceilometer captured a fog event where the cloud extends from the surface up to
343 around 130 m. The orbital imagery shows a fog bank extending from the shelf break up to the north of Sable
344 Island with weak southwesterly winds. Fog is visually observed on the south tower camera, though it is clearly
345 spatially inhomogeneous, as blue sky is visible on the top right corner of the image.
- 346 (ii) 07/10/2022 20:06 UTC: The fog bank has dissipated over the island, as shown in the ceilometer and visual obser-
347 vations. Nevertheless, camera imagery shows the presence of a fog bank off the island (in the horizon), consistent
348 with the orbital product still showing presence of fog around the island. It appears that fog has dissipated over
349 the island, as the land surface conditions experienced significant daytime warming, annihilating (locally) this fog
350 bank. Note the extent of the fog bank to the south starting to move south of the shelf break southeast of Sable
351 Island.
- 352 (iii) 07/10/2022 23:32 UTC: A well-defined fog bank has re-formed, extending from the surface to 90 m, more
353 homogeneous horizontally as compared to the observations earlier in the day.
- 354 (iv) 07/11/2022 01:01 UTC: During the earlier part of the evening, the height of the fog bank decreased to about
355 15 m at Sable Island. The lateral extent of the fog bank continues to follow the structure of the SST, ending at
356 the warmer water to the south. Fog droplets are visible in the camera imagery though interpretation is limited at
357 night.
- 358 (v) 07/11/2022 03:02 UTC: The fog bank started dissipating from the north, with no fog observed at Sable Island
359 from the camera and ceilometer.

360 In these observations of an individual fog event, we find that the fog extent follows the location of strong gradients
361 of SST more so than the location of the shelf break, in contrast to the statistics discussed in the previous sections.
362 The evolution of the fog cloud bank between the times presented in Figure 8(ii) and Figure 8(iii) shows the growth
363 of the cloud to start on the far side (offshore) once the air mass passes into the colder water pool off shelf. On the
364 northern side, we identify in Figure 8(iii) and (iv) where the fog begins to dissipate. The extent of the fog bank in
365 relation to surface temperature conditions is summarized in Figure 9. Here the location of the shelf break, the extent
366 of the fog probability of occurrence, and the percentage of time during which the fog persisted over a certain area is
367 plotted with different colors over the 48 hours of observation considered here. It can be seen that 17% of the time
368 or more (black contour), the fog stays primarily in the cold water, extending past the shelf break around -59°W . The
369 growth of the fog in the cold water areas hint at the rapid response to the change in the surface boundary conditions,
370 i.e. submesoscale features such as fronts and filaments, present near the shelf break. The changes in the surface
371 boundary conditions are likely affecting the marine boundary layer processes at play (Vrećica et al., 2022).

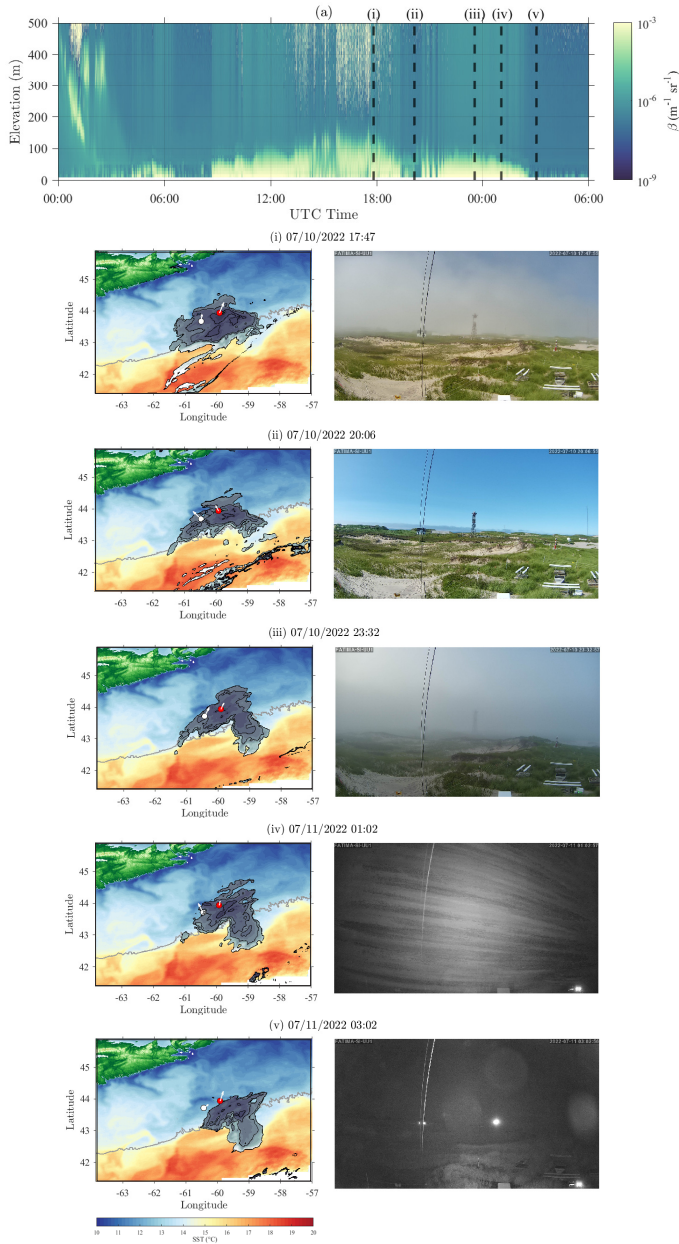


FIGURE 8 Fog characterization from GOES imagery over Sable Island from July 10-11, 2022. (a) Ceilometer data taken from the South Tower at Sable Island, (i)-(iv) (left) Satellite imagery of fog clouds where Sable Island is the red dot, the white dot is a waveglider, wind directions are shown by the arrows, and background mean SST is also plotted. Five specific times during the event are shown, correlating with the dashed lines in (a). (right) Visual imagery from a camera on the South Tower at Sable Island at similar times as the satellite imagery.

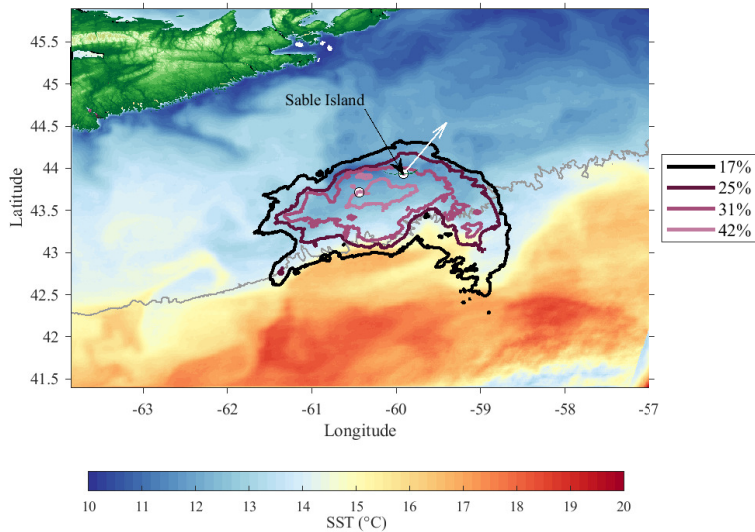


FIGURE 9 Fog persistence over the course of the 48 hour record of this individual fog event. Each contour shows the percentage of time that the fog persisted within the contour. The white arrow denotes average wind direction during these 48 hours. The 2000 m depth contour is shown in grey.

372 5 | CONCLUSIONS

373 In this study, we present a spatio-temporal climatology of fog probability of occurrence and its sufficient components
 374 in the Atlantic Canada region from 1950-2020. Using an archive of in-situ observations, reanalysis products, and
 375 remote sensing observations, we explore the influence of multi-scale air-sea interaction processes on the fog life
 376 cycle in the Grand Banks.

377 We show that fog occurs most during the summer months in the Atlantic Canada and Grand Banks region, highly
 378 concentrated along the continental shelf and correlated with the bathymetry. The fog probability of occurrence in-
 379 creases from May to July, reaching up to 60% in localized areas. In August, the probability decreases to below 40%,
 380 remaining concentrated on the shelf. Similarly, a strong negative air-sea temperature difference is also correlated with
 381 the bathymetry in this region. We find that the fog probability of occurrence increases as the magnitude of the air-sea
 382 temperature difference strengthens, as shown spatially in Figure 4 from May to July. As the fog occurrence decreases
 383 in August, the air-sea temperature difference becomes closer to 0. The highest occurrence coincides with an air-sea
 384 temperature difference between -2 to -4°C , as shown in Figure 5. Fog still occurs up to 50% of the time with a neutral
 385 and/or positive air-sea temperature difference, indicating that fog in this region is also driven by different mechanisms
 386 not explored here. Fog does not form in the southern part of this region, where the SST tends to be the warmest,
 387 around the Gulf Stream. The presence of an air-sea temperature difference is related to the stability of the marine
 388 boundary layer, as it aids or inhibits fog formation.

389 From an atmospheric perspective, two other essential conditions for fog formation include surface winds bringing

390 warmer air over the colder ocean region and the existence of low-level atmospheric temperature inversions above this
391 region. During the summer, winds on average are directed from the southwest, bringing warmer air from over the Gulf
392 Stream above the colder shelf water and Labrador Current waters to the north. From May to July, wind speeds tend
393 to increase (Figure 7g). From July to August, the wind speed decreases which points to a different mechanism causing
394 the fog occurrence to decrease. Above the surface, there is a high occurrence of low-level atmospheric temperature
395 inversions (over 70%) during the summer, which occurs primarily on the shelf. These inversions occur over 50% of the
396 time from May to August below a height of 500 m. Upwind of the shelf, the probability of occurrence of these low-
397 level inversions drops below 20% during the summer. The spatial and temporal consistency of these two parameters
398 with the air-sea temperature difference points to the prevalence of fog on the shelf during the summer.

399 Analysis of surface heat fluxes show another dimension of the air-sea interaction processes involved in the fog
400 life cycle in this area. Fog formation is associated with a positive surface latent heat flux, which is found to occur with
401 the same spatial pattern as the fog occurrence and the negative air-sea temperature difference. The sharp negative
402 to positive surface latent heat flux gradient across the shelf break shows the transition from evaporation to conden-
403 sation over a relatively short spatial scale of a few degrees latitude. The surface sensible heat flux associated with
404 fog dissipation follows this same pattern of a strong gradient along the shelf. The natural time scales of these two
405 processes are much smaller than what can be resolved by this analysis. Since these processes are also dependent on
406 the air-sea temperature differences, the spatial and temporal patterns are closely related.

407 From a climatological perspective, the consistent spatial distribution of the negative air-sea temperature differ-
408 ences, low-level atmospheric temperature inversions, and surface heat fluxes combined with the steady warm winds
409 create a region with an ideal setup for advection sea fog formation. Temporally, surface and atmospheric conditions
410 becomes ideal in the summer, particularly July, being the most probable month for fog occurring in the Grand Banks.
411 The ocean is a crucial boundary condition, as the air-sea temperature difference is the main factor in fog formation in
412 this region. The air-sea temperature difference is a product of the dynamic current interactions on the shelf from the
413 Gulf Stream and the Labrador Current and the steady warm winds flowing from the Gulf Stream. Additional studies
414 conducted on a smaller spatial and temporal scale exploring the impact of surface shelf water mixing on fog occurrence
415 aid in further understanding the role of the ocean on fog dynamics.

416 The relationship between the ocean and fog occurrence was explored during the fog event that occurred near
417 Sable Island. This analysis provided insight into the impact that sharp SST fronts have on fog. High-resolution satellite
418 imagery and in-situ observations of fog structure and winds during a specific fog event show how the fog cloud
419 was impacted by the ocean. As moist air passed over a sharp SST front, which was concurrent with the shelf break
420 bathymetry, a fog cloud formed and evolved over the region near Sable Island. The fog continued to build along the
421 SST front boundary, being advected to the northwest and dissipating along the further edge from the shelf break.
422 Over the 48 hour fog event, the southern boundary of the fog bank closely followed the boundary of the colder
423 water, which is mostly trapped on the shelf. We find here that the behavior of the fog event clearly depends on
424 the location of the SST front, which tends to follow the bathymetry in this region. This stresses the importance of
425 including accurate surface boundary conditions on the submesoscale when forecasting and modeling fog.

426 We find that this type of fog is dependent on ocean surface conditions and favorable atmospheric conditions.
427 Smaller-scale, accurate surface boundary conditions must be considered in modeling schemes to aid in precise fore-
428 casting of this phenomenon. Understanding fog dynamics in scales between the microphysical and synoptic ranges is
429 essential.

acknowledgements

This method of plotting uses the m-map plotting function from the University of British Columbia package made for MATLAB Pawlowicz (2020). We thank Sebastian Hoch at the University of Utah for providing the ceilometer data.

6 | SUPPORTING INFORMATION

Supporting information for this manuscript is available.

7 | DATA STATEMENT

The data that support the findings of this study are openly available in the UCSD Library Digital Collection at <https://doi.org/10.6075/JOD50N6F>.

references

Amani, M., Mahdavi, S., Bullock, T. and Beale, S. (2020) Automatic nighttime sea fog detection using goes-16 imagery. *Atmospheric Research*, **238**, 104712.

Bardoel, S., Hoch, S., Ruiz-Plancarte, J., Lenain, L., Gultepe, I., Grachev, A., Gaberseck, S., Wang, Q. and Fernando, H. J. (2024) Study of fog dissipation in an internal boundary layer on sable island.

Bower, A. S., Hendry, R. M., Amrhein, D. E. and Lilly, J. M. (2013) Direct observations of formation and propagation of subpolar eddies into the subtropical north atlantic. *Deep Sea Research Part II: Topical Studies in Oceanography*, **85**, 15–41.

Brodrick, C. (1907) Fog on the newfoundland banks. *Monthly Weather Review*, **35**, 76–78.

Byers, H. R. (1959) *General meteorology*. McGraw-Hill.

Chen, C., Zhang, M., Perrie, W., Chang, R., Gultepe, I., Fernando, H. J. and Chen, X. (2021) A case study: Evaluation of pafog one-d model with advection in simulations of fog/stratus from c-fog experiment. *Journal of Geophysical Research: Atmospheres*, **126**, e2021JD034812.

Clarke, R. A., Hill, H. W., Reiniger, R. F. and Warren, B. A. (1980) Current system south and east of the grand banks of newfoundland. *Journal of Physical Oceanography*, **10**, 25–65.

Dimitrova, R., Sharma, A., Fernando, H. J., Gultepe, I., Dančovski, V., Wagh, S., Bardoel, S. L. and Wang, S. (2021) Simulations of coastal fog in the canadian atlantic with the weather research and forecasting model. *Boundary-Layer Meteorology*, **181**, 443–472.

Dorman, C., Koračin, D., Gultepe, I., Hoch, S., Ruiz-Plancarte, J., Wang, Q., and Fernando, H. J. (2024) The role of the synoptic scale conditions in driving fog and mist during the fatima july 2022 sable island field program. Submitted.

Dorman, C. E., Hoch, S. W., Gultepe, I., Wang, Q., Yamaguchi, R. T., Fernando, H. and Krishnamurthy, R. (2021) Large-scale synoptic systems and fog during the c-fog field experiment. *Boundary-Layer Meteorology*, **181**, 171–202.

Dorman, C. E., Mejia, J., Koračin, D. and McEvoy, D. (2017) Worldwide marine fog occurrence and climatology. *Marine fog: Challenges and advancements in observations, modeling, and forecasting*, 7–152.

— (2020) World marine fog analysis based on 58-years of ship observations. *International journal of climatology*, **40**, 145–168.

- 462 Fallmann, J., Lewis, H., Sanchez, J. C. and Lock, A. (2019) Impact of high-resolution ocean–atmosphere coupling on fog forma-
463 tion over the north sea. *Quarterly Journal of the Royal Meteorological Society*, **145**, 1180–1201.
- 464 Fernando, H. J., Gultepe, I., Dorman, C., Pardyjak, E., Wang, Q., Hoch, S., Richter, D., Creegan, E., Gaberšek, S., Bullock, T. et al.
465 (2021) C-fog: life of coastal fog. *Bulletin of the American Meteorological Society*, **102**, E244–E272.
- 466 Fernando, H. J., Wang, S., Huang, K. Y. and Creegan, E. (2023) Fog-laden density staircases in the marine atmospheric boundary
467 layer. *Environmental Fluid Mechanics*, **23**, 489–510.
- 468 Fernando, J., Hoch, S., Gultepe, I., Dorman, C., Richer, D. and Shen, L. (2024) Fatima: Searching clarity within marine fog.
469 Submitted.
- 470 Findlater, J., Roach, W. and McHugh, B. (1989) The haar of north-east scotland. *Quarterly Journal of the Royal Meteorological
471 Society*, **115**, 581–608.
- 472 Fratantoni, P. S. and Pickart, R. S. (2007) The western north atlantic shelfbreak current system in summer. *Journal of Physical
473 Oceanography*, **37**, 2509–2533.
- 474 Freeman, E., Woodruff, S. D., Worley, S. J., Lubker, S. J., Kent, E. C., Angel, W. E., Berry, D. I., Brohan, P., Eastman, R., Gates, L.
475 et al. (2017) Icoads release 3.0: a major update to the historical marine climate record. *International Journal of Climatology*,
476 **37**, 2211–2232.
- 477 Grare, L., Statom, N. M., Pizzo, N. and Lenain, L. (2021) Instrumented wave gliders for air-sea interaction and upper ocean
478 research. *Frontiers in Marine Science*, **8**, 664728.
- 479 Gultepe, I., Pearson, G., Milbrandt, J., Hansen, B., Platnick, S., Taylor, P., Gordon, M., Oakley, J. and Cober, S. (2009) The fog
480 remote sensing and modeling field project. *Bulletin of the American Meteorological Society*, **90**, 341–360.
- 481 Gultepe, I., Tardif, R., Michaelides, S. C., Cermak, J., Bott, A., Bendix, J., Müller, M. D., Pagowski, M., Hansen, B., Ellrod, G.
482 et al. (2007) Fog research: A review of past achievements and future perspectives. *Pure and applied geophysics*, **164**,
483 1121–1159.
- 484 Han, G., Ma, Z., deYoung, B., Foreman, M. and Chen, N. (2011) Simulation of three-dimensional circulation and hydrography
485 over the grand banks of newfoundland. *Ocean Modelling*, **40**, 199–210.
- 486 Hersbach, H., Bell, B., Berrisford, P., Biavati, G., Horányi, A., Muñoz Sabater, J., Nicolas, J., Peubey, C., Radu, R., Rozum, I. et al.
487 (2018) Era5 hourly data on single levels from 1979 to present. *Copernicus climate change service (c3s) climate data store
488 (cds)*, **10**.
- 489 Hu, H., Zhang, Q., Xie, B., Ying, Y., Zhang, J. and Wang, X. (2014) Predictability of an advection fog event over north china.
490 part i: Sensitivity to initial condition differences. *Monthly Weather Review*, **142**, 1803–1822.
- 491 Hu, R. and Zhao, J. (2022) Sea surface salinity variability in the western subpolar north atlantic based on satellite observations.
492 *Remote Sensing of Environment*, **281**, 113257.
- 493 Isaac, G. A., Bullock, T., Beale, J. and Beale, S. (2020) Characterizing and predicting marine fog offshore newfoundland and
494 labrador. *Weather and Forecasting*, **35**, 347–365.
- 495 Koračin, D. and Dorman, C. E. (2017) *Marine fog: challenges and advancements in observations, modeling, and forecasting*.
496 Springer.
- 497 Koračin, D., Dorman, C. E., Lewis, J. M., Hudson, J. G., Wilcox, E. M. and Torregrosa, A. (2014) Marine fog: A review. *Atmo-
498 spheric Research*, **143**, 142–175.
- 499 Loder, J. (1998) The coastal ocean off northeastern north america: A large-scale view. *The sea*, **11**, 105–133.

- 500 Lumpkin, R. and Centurioni, L. (2019) Global drifter program quality-controlled 6-hour interpolated data from ocean surface
501 drifting buoys. URL: <https://doi.org/10.25921/7ntx-z961>.
- 502 Mahdavi, S., Amani, M., Bullock, T. and Beale, S. (2020) A probability-based daytime algorithm for sea fog detection using
503 goes-16 imagery. *IEEE Journal of Selected Topics in Applied Earth Observations and Remote Sensing*, **14**, 1363–1373.
- 504 McWilliams, J. C. (2016) Submesoscale currents in the ocean. *Proceedings of the Royal Society A: Mathematical, Physical and
505 Engineering Sciences*, **472**, 20160117.
- 506 Nieuwstadt, F. (2005) The atmospheric boundary layer. In *Environmental Stratified Flows*, 179–232. Springer.
- 507 Park, S.-Y., Yoo, J.-W., Song, S.-K., Kim, C.-H. and Lee, S.-H. (2022) Numerical study on advective fog formation and its
508 characteristic associated with cold water upwelling. *Plos one*, **17**, e0267895.
- 509 Pawlowicz, R. (2020) M-map: A mapping package for matlab. URL: www.eoas.ubc.ca/~rich/map.html.
- 510 Petrie, B. and Anderson, C. (1983) Circulation on the newfoundland continental shelf. *Atmosphere-Ocean*, **21**, 207–226.
- 511 Pithani, P., Ghude, S. D., Chennu, V. N., Kulkarni, R. G., Steeneveld, G.-J., Sharma, A., Prabhakaran, T., Chate, D., Gultepe, I.,
512 Jenamani, R. et al. (2019) Wrf model prediction of a dense fog event occurred during the winter fog experiment (wifex).
513 *Pure and Applied Geophysics*, **176**, 1827–1846.
- 514 Richardson, P. L., Steele, J., Thorpe, S. and Turekian, K. (2001) Florida current, gulf stream, and labrador current. *Ocean currents*,
515 13–22.
- 516 Ricketts, N. G., Trask, P. D., Smith, E. H., Soule, F. M., Mosby, O., Institution., W. H. O. and Guard., U. S. C. (1931) *The
517 "Marion" expedition to Davis Strait and Baffin Bay : under direction of the United States Coast Guard, 1928. Scientific re-
518 sults, vol. pt.1. Washington, U.S. Govt. Print. Off, 1931-37. URL: <https://www.biodiversitylibrary.org/item/41867>.
519 <https://www.biodiversitylibrary.org/bibliography/10182>.*
- 520 Scoresby, W. (1823) *Journal of a voyage to the northern whale-fishery: including researches and discoveries on the eastern coast of
521 West Greenland, made in the summer of 1822, in the ship Baffin of Liverpool*, vol. 125. Edinburgh: Printed for A. Constable.
- 522 Severini, M., Tonna, G., Moriconi, M. et al. (1986) Determination of the latent heat flux in fog. *Atmospheric Environment (1967)*,
523 **20**, 397–400.
- 524 Sheng, J. and Thompson, K. R. (1996) Summer surface circulation on the newfoundland shelf and grand banks: The roles of
525 local density gradients and remote forcing. *Atmosphere-Ocean*, **34**, 257–284.
- 526 Skyllingstad, E. D., Vickers, D., Mahrt, L. and Samelson, R. (2007) Effects of mesoscale sea-surface temperature fronts on the
527 marine atmospheric boundary layer. *Boundary-layer meteorology*, **123**, 219–237.
- 528 Su, Z., Wang, J., Klein, P., Thompson, A. F. and Menemenlis, D. (2018) Ocean submesoscales as a key component of the global
529 heat budget. *Nature communications*, **9**, 775.
- 530 Talley, L. D. (2011) *Descriptive physical oceanography: an introduction*. Academic press.
- 531 Taylor, G. (1917) The formation of fog and mist. *Quarterly Journal of the Royal Meteorological Society*, **43**, 241–268.
- 532 Taylor, P. A., Chen, Z., Cheng, L., Afsharian, S., Weng, W., Isaac, G. A., Bullock, T. W. and Chen, Y. (2021) Surface deposition of
533 marine fog and its treatment in the weather research and forecasting (wrf) model. *Atmospheric Chemistry and Physics*, **21**,
534 14687–14702. URL: <https://acp.copernicus.org/articles/21/14687/2021/>.
- 535 Thompson, W. T., Burk, S. D. and Lewis, J. (2005) Fog and low clouds in a coastally trapped disturbance. *Journal of Geophysical
536 Research: Atmospheres*, **110**.

- 537 Vrećica, T., Pizzo, N. and Lenain, L. (2022) Observations of strongly modulated surface wave and wave breaking statistics at a
538 submesoscale front. *Journal of Physical Oceanography*, **52**, 289–304.
- 539 Wainwright, C. and Richter, D. (2021) Investigating the sensitivity of marine fog to physical and microphysical processes using
540 large-eddy simulation. *Boundary-Layer Meteorology*, **181**, 473–498.
- 541 Willett, H. C. (1928) Fog and haze, their causes, distribution, and forecasting. *Monthly weather review*, **56**, 435–468.
- 542 WMO (2019) *Manual on Codes*. No. v. 1 in Manual on Codes. Secretariat of the World Meteorological Organization. URL:
543 <https://library.wmo.int/idurl/4/35713>.
- 544 Yang, Y. and Gao, S. (2020) The impact of turbulent diffusion driven by fog-top cooling on sea fog development. *Journal of*
545 *Geophysical Research: Atmospheres*, **125**, e2019JD031562.
- 546 Yang, Y., Hu, X.-M., Gao, S. and Wang, Y. (2019) Sensitivity of wrf simulations with the ysu pbl scheme to the lowest model
547 level height for a sea fog event over the yellow sea. *Atmospheric Research*, **215**, 253–267.
- 548 Yun, J. and Ha, K.-J. (2022) Physical processes in sea fog formation and characteristics of turbulent air-sea fluxes at socheong-
549 cho ocean research station in the yellow sea. *Frontiers in Marine Science*, **9**, 825973.
- 550 Zhang, S.-P., Xie, S.-P., Liu, Q.-Y., Yang, Y.-Q., Wang, X.-G. and Ren, Z.-P. (2009) Seasonal variations of yellow sea fog: Obser-
551 vations and mechanisms. *Journal of Climate*, **22**, 6758–6772.
- 552 Zuo, H., Balmaseda, M. A., Mogensen, K. and Tietsche, S. (2018) Ocean5: the ecmwf ocean reanalysis system and its real-time
553 analysis component.